Materials Futures

In situ active guanidinium salts interaction promotes facet orientation and crystallization for efficient and stable inverted perovskite solar cells

To cite this article before publication: Jiajia Du *et al* 2025 *Mater. Futures* in press https://doi.org/10.1088/2752-5724/ae0c77

In situ active guanidinium salts interaction promotes facet orientation and crystallization for efficient and stable inverted perovskite solar cells

Journal:	*Materials Futures*
Manuscript ID	MF-100890.R1
Manuscript Type:	Paper
Date Submitted by the Author:	22-Sep-2025
Complete List of Authors:	Du, Jiajia; Tianjin University of Technology; Shandong University - Qingdao Campus Chang, Yilin; Shandong University - Qingdao Campus Liu, Le; Shandong University - Qingdao Campus Yu, Zhibin; Shandong University - Qingdao Campus Du, Qinglin; Shandong University - Qingdao Campus Yang, Wenfeng; Shandong University - Qingdao Campus Qiu, Yuan; Tianjin University of Technology Lu, Fushen; Shantou University Jiu, Tonggang; Shandong University - Qingdao Campus Cao, Huanqi; Tianjin University of Technology,
Keywords:	in situ reaction, guanidine synthesis, crystallization orientation, α-phase stabilization, inverted perovskite solar cells

In situ active guanidinium salts interaction promotes facet orientation and crystallization for efficient and stable inverted perovskite solar cells

Jiajia Du[1,2,†], Yilin Chang[2,†], Le Liu[2,3,*], Zhibin Yu[2], Qinglin Du[2], Wenfeng Yang[2], Yuan Qiu[1], Fushen Lu[4,*], Tonggang Jiu[2,*], Huanqi Cao[1,*]

[1] Key Laboratory of Display Materials and Photoelectric Devices (Ministry of Education), Tianjin Key Laboratory for Photoelectric Materials and Devices & National Demonstration Center for Experimental Function Materials Education, School of Materials Science and Engineering, Tianjin University of Technology, Tianjin 300384, P. R. China.

[2] Shandong Provincial Key Laboratory for Science of Material Creation and Energy Conversion, Institute of Frontier Chemistry, School of Chemistry and Chemical Enginnering, Shandong University, Qingdao, 266237, P. R. China.

[3] Shenzhen Research Institute of Shandong University, Shenzhen, 518057, China.

[4] College of Chemistry and Chemical Engineering, and Key Laboratory for Preparation and Application of Ordered Structural Materials of Guangdong Province, Shantou University, Shantou, Guangdong 515063, China.

E-mail addresses: liule@sdu.edu.cn, fslu@stu.edu.cn, tgjiu@sdu.edu.cn and caoh@tjut.edu.cn.

† These authors contribute equally to this work.

Supplementary material for this article is available online.

Abstract: The disordered crystal growth and undesired degradation of perovskite films limit the further improvement of perovskite solar cells (PSCs) performance and their commercialization. Herein, an in situ modulation strategy is proposed for preparing high-quality and stable perovskite film through adjustment of phase transformation kinetics. Benefiting from the in situ reaction between chloroformamidinium hydrochloride (ClFACl) and FA cations, the impurity intermediate phase in the perovskite film is inhibited and the α-$FAPbI_3$ phase is induced to grow along a preferred (001) orientation. Furthermore, the introduction of ClFACl and in situ formation of guanidinium salts (FA-Gua) strengthen the intermolecular interactions in the interior of crystals, which restrains the α-phase degradation of the as-prepared perovskite films under humid and thermal treatments. With crystal orientation optimization and defects reduction, the PSCs with in situ formed FA-Gua yield a champion efficiency of 25.85% and demonstrate excellent phase stability under long-term thermal and humid ageing conditions. This in situ chemical modulation strategy expands the avenue toward optimization of crystallization orientation and α-phase stabilization, promoting the development of PSCs with enhanced performance and stability.

Keywords: in situ reaction, guanidine synthesis, crystallization orientation, α-phase stabilization, inverted perovskite solar cells

1. Introduction

Metal halide perovskites have become one of the most promising semiconductors in the field of optoelectronics [1,2]. Among them, Formamidine (FA)-dominant perovskite solar cells (PSCs) have garnered tremendous interest due to the ongoing improvement of photoelectric property, which show great potential in practical commercialization [3-10]. However, the PSCs based on polycrystalline perovskite films still face the phase and environmental instability problem [11-16]. The overall quality of perovskite films is pivotal in phase instabilities, especially for high defect state density derived from disordered crystal growth orientation due to rapid uncontrolled crystallization process [17-24]. Therefore, it is of great significance to manipulate facet orientation during fast crystallization processes to reduce defect density and obtain high-performance and stable perovskite solar cells [25-27].

To date, substantial research strategies have been used to regulate perovskite films crystallization orientation, while the relevance between the facet orientations of perovskite films and corresponding device photovoltaic performance has been widely investigated [28-31]. Recently, preferential growth of (001) and (111) facets has received much attention, since these two facets have both been proved to be the top-performing ones [32-37]. Compared with the (111) facet, the (001) facet possesses more closely connected atoms, exhibiting lower surface energy, better coordination balance and less defects [32,37,38]. Various efforts have been devoted to realizing the favourable growth of the (001) facet, especially by regulating crystal orientation and passivating defects both in the bulk and at the interface, such as composition engineering [27,29,39,40], processing management [41,42], additive engineering [37,43], etc. For example, highly oriented 2D (BDA)PbI_4 (1,4-butanediamine) seeds were used to customize the facet orientation of 3D perovskite, so that the preferential growth of (001) and (002) facets were promoted [37], However, the weak Pb-I bond brings about structural distortion and the high

sensitivity of the (001) facet toward water molecules entails severe moisture-induced degradation [44], Although electric carriers transport is facilitated along the (001) direction, the octahedral interstices that extend through the crystal in this direction also facilitates the escape of the A-site cations, largely lowering device stability. Therefore, it is of essential importance to explore a new way to further strengthen the intermolecular interactions in the interior of crystals as well as capping the (001) layers for stability enhancement of facet-oriented perovskite films.

In this work, we proposed an in situ modulation strategy based on guanidinium salts prepared by the interaction between chloroformamidine hydrochloride (ClFACl) and FA cations in the perovskite precursor. It is demonstrated that the in situ reaction between ClFACl and FA cations effectively promotes the transformation of perovskite intermediate phase to α-$FAPbI_3$ and inhibits the impurity phase in the perovskite film, which is favourable for the selective crystal growth along the (001) crystal plane. More importantly, by taking benefits of the interaction between as-formed active guanidinium salts and perovskite, the intermolecular interactions in the interior of crystals are strengthened, which retards the degradation of the α-$FAPbI_3$ phase under high humidity and elevated temperature conditions. Furthermore, the optimized perovskite films deliver reduced defects and suppressed trap-assisted non-radiative recombination. Therefore, profiting from the in situ reaction and active guanidinium salts, the PSCs achieved a champion PCE of 25.85% with an optimized open-circuit voltage (V_{OC}) of 1.21 V. In addition, perovskite films with active guanidinium salts show excellent stability under long-term thermal and humid ageing conditions, the unencapsulated devices retained 95% of the initial PCE after storage in the N_2 atmosphere for 2000 h. Our findings provide a new perspective to preparing highly facet-oriented and stable perovskite films for construction of efficient and stable PSCs.

2. Experimental section

2.1 Materials

Chloroformamidine hydrochloride (ClFACl) and Formamidine iodide (FAI) were obtained from Greatcell Solar Materials. Lead (II) iodide (PbI_2) and (2-(9H-carbazol-9-yl) ethyl) phosphonic acid (2PACz) were purchased from Tokyo Chemical Industry Co., Ltd. Lead bromide ($PbBr_2$), methylammonium bromide (MABr), phenylethyl ammonium iodide (PEAI), methyl ammonium chloride (MACl) and phenyl-C_{61}-butyric acid methyl ester ($PC_{61}BM$) were procured from Xian Yuri Solar Co., Ltd. Cesium iodide (CsI), N,N-dimethylformamide (DMF), dimethylsulfoxide (DMSO) and chlorobenzene (CB) were provided by Sigma-Aldrich Corp. Ethyl alcohol was obtained from J&K. Isopropanol (IPA) and bathocuproine (BCP) were purchased from Aladdin. SnO_2 colloid precursor was purchased from Alfa Aesar (tin (IV) oxide, 15 wt.% in H2O colloidal dispersion). 2,2″,7,7″-Tetrakis[N, N-di(4-methoxyphenyl) amino]-9,9″-spirobifluorene;2,2″,7,7″-Tetrakis (N, N-p-dimethoxyphenylamino)-9,9-spirobifluoree (Spiro-OMeTAD) was purchased from Xi'an Polymer Light Technology Corp. These materials were used without additional processing.

2.2 Preparation of pristine and additive-doped perovskite precursor solutions

The FA-based perovskite precursor solution was prepared by dissolving 5.0 mg of MACl, 13.4 mg of $PbBr_2$, 4 mg of MABr, 8.9 mg of CsI, 240.1 mg of FAI and 725.8 mg of PbI_2 in 1000 μL of anhydrous DMF/DMSO (volume ratio 4:1) mixed solvent. The optimized perovskite precursor was obtained by added different concentrations of ClFACl (0.5~1 mg mL^{-1}) to the perovskite solution.

2.3 Device fabrication

The inverted (p-i-n) perovskite solar cell prepared in this paper had the structure of ITO/2PACz/perovskite/$PC_{61}BM$/BCP/Ag. Firstly, the ITO substrates were ultrasonically cleaned for 15 min with glass cleaner, deionized water, acetone and IPA respectively and treated by plasma for 15 min. Then, the as-cleaned ITO substrates were transferred to the glovebox and 2PACz (0.5~1.5 mg mL^{-1}) in ethyl alcohol was spin-coated on cleaned ITO substrates and annealed for 10 min under 100 °C. The as-prepared perovskite precursor solution was spin-coated onto the 2PACz substrates by two step program of 1000 rpm for 5 s and 4000 rpm for 30 s, with a ramping rate of 1000 rpm s^{-1}. During the last 5~10 s of the spinning process, the liquid film was treated by drop-casting of chlorobenzene solvent (250 μL). The perovskite solution with ClFACl additive took the same process and was annealed on a hotplate at 100 °C for 50 min. After the perovskite films cooled down, PEAI solution (2 mg mL^{-1}) was spin-coated on top of perovskite films surface at a speed of 4000 rpm for 20 s. Then, A $PC_{61}BM$ layer (20 mg mL^{-1} in chlorobenzene, 2500 rpm for 20 s) was spin-coated and annealed for 10 min under 100 °C, followed by spin-coating with BCP (0.5~1.0 mg mL^{-1}) in isopropanol on top (4000 rpm, 30 s). Finally, the 100 nm thick Ag electrode layer was deposited on top by thermal evaporation.

2.4 Characterizations

The FT-IR spectra were obtained with a spectrometer of Agilent Technologies (Cary 630 KBr Engine). GISAXS measurements were carried out on Anton Paar SAXS point 5.0. The Bruke D8 Advance X-ray Diffractometer with Cu Kα radiation from 4° to 45° was used to record XRD patterns. The ^{1}H NMR spectra were obtained with Ascend TM 600 MHz nuclear magnetic resonance spectrometer. The XPS and UPS spectra were obtained by Thermo scientific EscaLab

250Xi. AFM/KPFM (Bruker MultiMode 8) and SEM (Thermo scientific, Apreo) were applied to observe the film morphology. PL and TRPL spectra were obtained at room temperature through fluorescent spectrophotometer (Edinburgh FS5) equipped with a 500 W Xe lamp. Confocal laser scanning microscopy (Leica DM18) was used to record PL mapping. The TPC/TPV decays were determined by all-in-one characterization platform Paios (Fluxim AG, Switzerland). The EIS measurement was performed using a Chi760e electrochemical workstation. The Powereach JC 2000C was used to record contact angles. The simulated AM 1.5G solar illumination (100 mW cm^{-2}) with an Enlitech solar simulator (SS-F5-3A) and a computer-controlled Keithley 2400 source meter was used to detect the current density–voltage (*J–V*) characterizations of perovskite solar cells.

2.5 Density functional theory (DFT) simulations

All calculations in this work were done with using the Vienna ab initio simulation package (VASP). The exchange energy and correlation energy of electrons are described using the generalized gradient approximation (GGA) with the Perdew Burke Ernzerhof (PBE) function. In the calculation, a cutoff energy of 450 eV was set for the plane wave basis set. The force convergence standard for each atom is set to 0.02 eV/Å. The binding energies of the molecule on α-$FAPbI_3$ surfaces were calculated to investigate their interactions. To avoid interactions between adjacent slabs, a vacuum layer of more than 20 Å is added to the surface in the 2D slab model. The binding energy (E_b) is based on the following equation:

$$E_b = E_{molecule\text{-}slab} - E_{molecule} - E_{slab}$$

Where $E_{molecule\text{-}slab}$, $E_{molecule}$ and E_{slab} are the energy of the FA-Gua molecule adsorbed on the α-$FAPbI_3$ surface, individual FA-Gua molecule, and the clean α-$FAPbI_3$ surface, respectively.

3. Results and discussion

As shown in figure 1(a), we introduced ClFACl into the perovskite precursor solution to regulate the crystallization of perovskite film, taking advantage of active guanidinium salt produced via an in situ reaction. The amino-group-rich active guanidine would strongly interact with halide ion and uncoordinated Pb^{2+} through electrostatic coupling and/or hydrogen bonds, inducing the highly-oriented crystallization of perovskite films [45]. To study the chemical interaction between ClFACl and perovskite precursors and confirm the production of active guanidine, proton nuclear magnetic resonance (^{1}H NMR) measurement was employed. As shown in figure 1(b), the chemical shifts of the hydrogen atoms for ─CH and ─NH/=NH in FAI are identified as two proton peaks at 7.84 and 8.82 ppm, respectively, while the proton peak for ClFACl can be detected at 6.21 ppm. Upon the addition of ClFACl into the FAI solution, the solution turned yellow (interior picture in figure 1(b) and S1), indicating a reaction occurred between the ClFACl and FAI. After FAI and ClFACl were mixed, the ^{1}H NMR signals of ─CH in FA^+ split into a multiple peaks and three proton peaks at 8.68, 8.87 and 9.11 ppm appeared with the integration ratio of 1: 1: 2: 2 (a: c: b: d) (figure S2), which indicates strong chemical interaction between FAI and ClFACl and a guanidinium salt was synthesized. Moreover, as shown in figure S3, compared with the X-ray diffraction (XRD) patterns of FAI and ClFACl, the ClFACl/FAI mixture showed characteristic peaks at 11.46° and 22.67°, which demonstrates that FA-Gua crystals with different face orientations were formed. Based on the ^{1}H NMR results and considering the deprotonation of organic amidines and the potential of amidines as guanylating agents [46], it could be proved that FAI was firstly deprotonated, then a nucleophilic substitution reaction took place between FA and ClFACl to yield active guanidine. The reaction process between ClFACl and FAI for guanidine synthesis (FA-Gua) is displayed in Scheme 1.

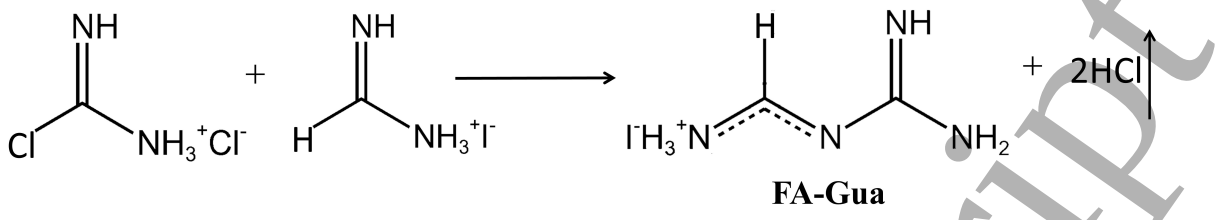

Scheme 1. The proposed reaction process between ClFACl and FAI in perovskite precursor solution.

The in-situ formation of FA-Gua was further verified by ^{1}H NMR spectroscopy. As shown in figure S4, FAI/ClFACl/PbI_2 in one-step blending showed the same phenomenon as after FAI/ClFACl pre-reaction purification, with the original proton peak at 7.84 ppm of FAI splitting into multiple peaks. And the proton peak at 8.82 ppm disappeared, with a new doublet peak at 8.65 and a new singlet peak at 8.99 ppm. On the contrary, when FAI and PbI_2 are mixed, the proton peak at 7.84 ppm does not split, and the proton peak belonging to ─NH at 8.82 ppm splits into two single peaks (no doublet peak at 8.65 ppm). The results show that ClFACl tends to react with FAI to form active guanidine, and then coordinates with PbI_2 to form complex to further regulate crystal growth in mixed perovskite precursor solution.

The strong interaction between ClFACl and FAI is further verified via fourier-transform infrared spectroscopy (FT-IR, figure 1(c)) and X-ray photoelectron spectroscopy (XPS) measurements. As displayed in figure 1(c), the stretching vibration peaks of $\nu_{C\text{-}Cl}$, $\nu_{C\text{-}N}$, $\nu_{N\text{-}H}$ for ClFACl are located at 674.64, 1416.09 and 3020.86 cm^{-1}, respectively. After mixed with FAI, the stretching vibration peaks shifted to 622.46, 1343.71 and 3140.28 cm^{-1}, respectively. Meanwhile, as depicted in the XPS spectra (figure S5), compared with pure ClFACl, the N 1s peak of ClFACl/FAI mixture show a shift from 400.15 eV to a slightly higher binding energy of

400.49 eV. These results indicate the strong interaction between ClFACl and FAI, and indicating the foramation of FA-Gua.

In addition, the interaction between ClFACl and PbI_2 was also investigated by FT-IR. As exhibited in the FT-IR results (figure S6), the ν_{N-H} stretching vibration peak of ClFACl shifted from 3020.86 to 3137.36 cm^{-1} for ClFACl/PbI_2 mixture and to 3267.44 cm^{-1} for FAI/ClFACl/PbI_2 mixture. The shift of ν_{N-H} is due to the formation of coordination bonds between FA-Gua and PbI_2, indicating the stronger coordination of in situ synthesized FA-Gua with Pb^{2+} [47]. Furthermore, as shown in the XPS spectra of I 3d and Pb 4f signals (figure 1(d) and 1(e)), compared with pure PbI_2 (143.58 eV for Pb 4f and 631.06 eV for I 3d), the ClFACl/PbI_2 film exhibited lower binding energies of Pb 4f (143.35 eV) and I 3d (630.26 eV), while further shifts were observed for FAI/ClFACl/PbI_2 (143.06 eV for Pb 4f and 630.01 eV for I 3d). The further reduction of binding energies demonstrates that the intermolecular interaction between the organic cations and PbI_2 was strengthened with in situ synthesis of FA-Gua [48-50]. Therefore, to investigate the effect of in situ guanidine synthesis on the final perovskite film, we recorded the XPS spectra of the as-prepared perovskite films, as exhibited in figure 1(f)-(h). The ClFACl-treated film displayed two peaks at 142.91 and 138.04 eV, corresponding to Pb $4f_{5/2}$ and $4f_{7/2}$, respectively, which are lower than those of the pristine one (143.27 and 138.41 eV). Moreover, the two peaks belonging to Pb^0 at 141.69 and 136.77 eV disappeared for ClFACl-treated film, indicating the suppression of less-coordinated Pb atoms in the optimized film. Meanwhile, the signals of I $3d_{3/2}$, I $3d_{5/2}$ and N 1s all showed obvious shifts to lower binding energies after ClFACl treatment, owing to the electron donation effect of FA-Gua.

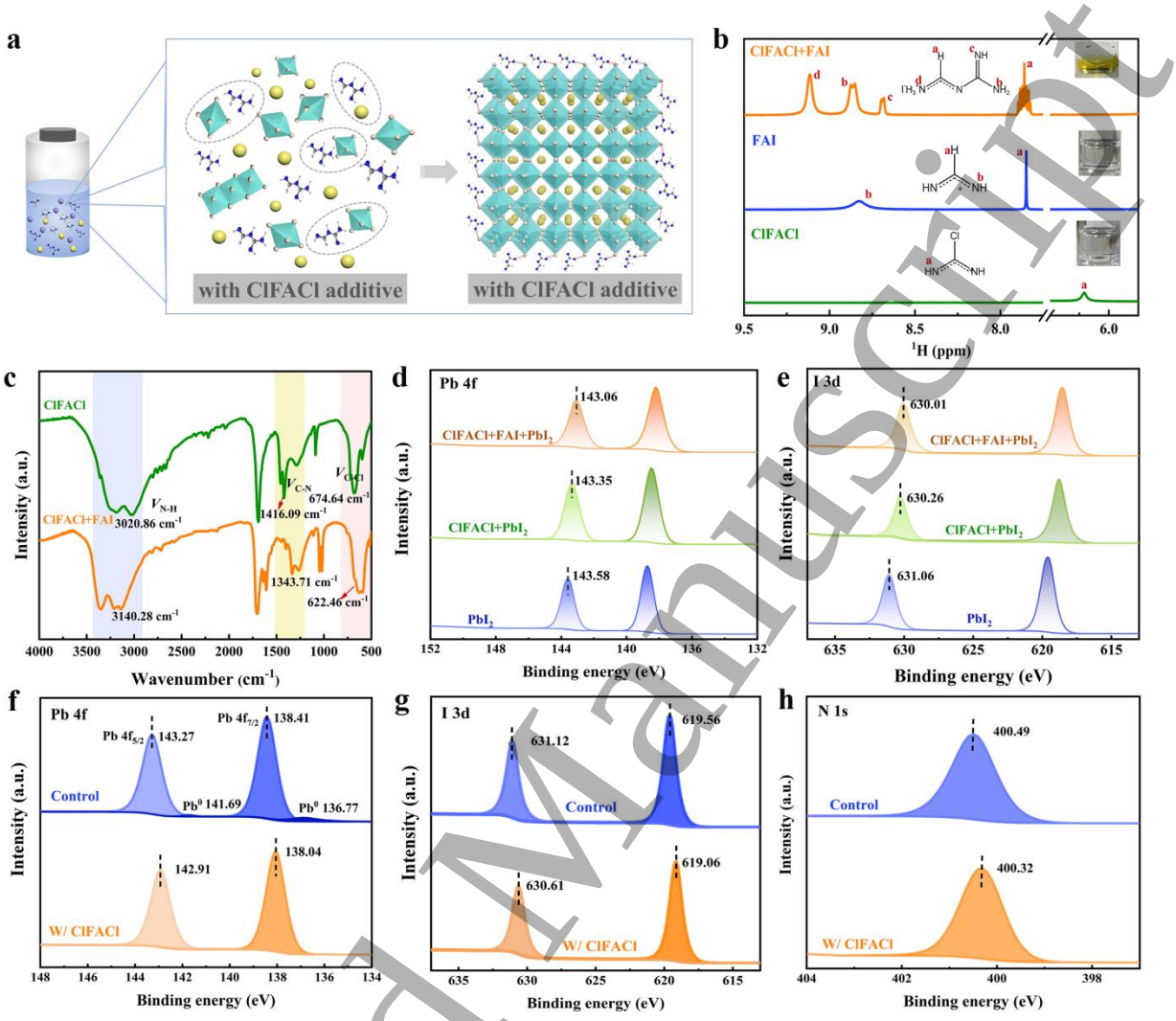

Figure 1. Additive and perovskite interaction analysis. (a) Schematic diagram of intermolecular interaction between ClFACl and perovskite components for crystallization regulation. (b) ^{1}H NMR spectra of the ClFACl, ClFACl and FAI/ClFACl mixture in DMSO-D_6. (c) FTIR spectra of ClFACl and FAI/ClFACl mixture. (d-e) Pb 4f and I 3d XPS spectra of PbI_2, ClFACl/PbI_2 mixture and ClFACl/FAI/PbI_2 mixture. (f-h) Pb 4f, I 3d and N 1s XPS spectra of perovskite films with and without ClFACl treatment.

Dynamic light scattering (DLS) was used to investigate the effect of ClFACl on the sizes of colloidal particles in perovskite precursor solution. As presented in figure S7, the ClFACl-

treated perovskite solution shows more homogeneous colloidal sizes than the pristine solution. With the introduction of ClFACl, the larger agglomerative particles in perovskite solution are broken, benefiting from the hydrogen bonds and coordination interaction between FA-Gua and perovskite. The perovskite solution with a larger and homogeneous colloidal size is beneficial to homogeneous nucleation of the film during the spin-coating process, in favor of obtaining increased crystal size and high-quality perovskite films [51,52]. Meanwhile, the ClFACl-treated perovskite solution show a larger contact angel (25°) than that of the pristine one (16°) on 2-(9H-Carbazol-9-yl)ethyl]phosphonic acid (2PACz) substrate, which is beneficial to the formation of perovskite films with larger crystals (figure S8) [53,54].

XRD measurement was employed to detect detailed crystal growth processes under different annealing temperatures. As shown in figure S9, for the control perovskite film, obvious diffraction peaks of δ-$FAPbI_3$ and PbI_2 phases were observed at 11.9° and 12.8°, respectively, while a weaker signal of α-$FAPbI_3$ phase was found at 14.2° under low-temperature annealing conditions. The peak intensity corresponding to the α-$FAPbI_3$ phase increased slowly with the increase of annealing temperature. In contrast, for the ClFACl-treated perovskite film, the diffraction peak of α-$FAPbI_3$ phase was strong even under low-temperature and increased further after annealing at higher temperatures, while the peaks of δ-$FAPbI_3$ phase and PbI_2 are suppressed dramatically.

In addition, the XRD patterns of perovskite films without antisolvent dripping and annealing treatment are displayed in figure S10. For the pristine perovskite film, the peaks at 6.89° and 14.28° could be assigned to a $FA_2Pb_3I_8{\cdot}4DMSO$ intermediate phase and the α-$FAPbI_3$ phase, respectively [55]. With ClFACl-treated processing, the peak intensity of the intermediate phase decreased and the peak intensity of α-$FAPbI_3$ was greatly enhanced, indicating that the

introduction of ClFACl could inhibit the formation of the impurity intermediate phase and promote the formation of the α-$FAPbI_3$ phase.

Moreover, as presented in the XRD patterns of the as-prepared perovskite films (figure 2(a) and 2(b)), the diffraction peaks at 12.89°, 14.35° and 40.75° correspond to PbI_2, (001) and (022) crystal facets of the α-$FAPbI_3$ phase, respectively. The intensity of (001) diffraction peak for ClFACl-treated perovskite film increased by 2.83 times than that of the pristine one. The ratio of $I_{(001)}/I_{(022)}$ rose to 7.12 and the ratio of $I_{PbI2}/I_{(001)}$ decreased to 0.03 for ClFACl-treated perovskite film, indicating that the in situ formation of FA-Gua promoted the crystal orientation growth along with the preferred (001) direction effectively and improve the crystallinity of the perovskite film.

XRD refinement further proves this point and the results are shown in figure S11. R_{wp} is Weighted Profile Residual Factor for XRD Rietveld refinement. It can be calculated by the following formula:

$$R_{wp} = [\frac{\sum w_i(y_{io} - y_{ic})^2}{\sum w_i y_{io}^2}]^{0.5}$$

where, y_{io} is the experimentally observed intensity of the i-th data point, y_{ic} is the theoretical intensity of the i-th data point calculated based on the refined model, and w_i is the weight of the i-th data point. A smaller R_{wp} value indicates a higher degree of agreement between the theoretical calculated spectrum and the experimental spectrum [56]. Firstly, from the refinement results, it can be seen that the lattice parameters of the perovskite film containing FA-Gua are the same as those of the control film, and the variation is within an allowable range, indicating that the in-situ generated FA-Gua did not enter the lattice interior. Secondly, the characteristic peak

positions of the XRD diffraction patterns of the perovskite films before and after refinement are in good agreement, and the R_{wp} (5.90%) of the perovskite film containing FA-Gua is much smaller than that of the control film (6.99%), indicating that the crystallinity of the perovskite after ClFACl treatment is better.

The grazing-incidence wide-angle X-ray scattering (GIWAXS) patterns at incident angels ranging from 0.3° to 3.6° for control and ClFACl-treated perovskite films were tested to further elucidate the impact of in situ synthesized FA-Gua on the crystalline structure of perovskite films. As shown in figure 2(c), 2(d) and S12, compared with the control film, the signal of PbI_2 decreased significantly and a visibly preferred crystallographic orientation along with (001) facet is observed for the ClFACl-treated film with the increase of incident angle. The results are consistent with the conclusion of XRD, suggesting the selective facet growth and regular crystalline arrangement of perovskite crystals after the ClFACl additive treatment. Meanwhile, the radially integrated intensity along the ring at $q \approx 10$ nm^{-1} with an incident angle of 3.6° is displayed in figure S13, revealing that the (001) facet of ClFACl-treated perovskite film exhibits strong out-of-plane (OOP) orientation. Furthermore, Williamson–Hall (W–H) plots extracted from XRD pattern were further adopted to show the lattice strain of the perovskite films. The lattice strain ε of the films can be extracted from XRD patterns by fitting the slope in the Williamson-Hall plot: $\beta \cos\theta = 4\varepsilon \sin\theta + k\lambda/D_{size}$, where, β represents the half-width of the diffraction peak (unit: radian). θ is the diffraction angle. k is a constant (Scherrer constant, usually taken as 0.9). λ is the wavelength of X-rays. D is the average size of the crystal grains, and ε is the lattice strain. sinθ is the sine value of the diffraction angle. As shown in Figure S14, it can be seen that the perovskite film prepared with FA-Gua show the lowest strain of -0.003% compared with control perovskite film (-0.036%). The small lattice strain could be attributed to

the FA-Gua that guide the homogeneous crystal growth and the enhanced orientation that reduces the collision volume between grains when forming crystals [57].

To better investigate the advantages of in-situ synthesis of FA-Gua and exclude chloride ion effects on perovskite growth, we selected FA-Gua structural analogs N-(diaminomethylidene) methanimidamide (N-DM), 1,1-dimethylbiguanide Hydrochloride (DH-Gua), and HCl as control additives. X-ray diffraction (XRD) tests were conducted on corresponding perovskite films. As shown in figure S15, the control perovskite films exhibited a disordered crystal orientation with residual lead iodide and δ-phase $FAPbI_3$ at 11.7°. The DH-Gua-containing perovskite films displayed low-dimensional perovskite characteristic peaks at low angles and no significant improvement in crystal orientation. The perovskite films containing an equal molar amount of hydrochloric acid exhibited the same crystallinity as the control films, indicating that the introduction of chloride ion had no effect on the crystal growth orientation. Notably, perovskite films with N-DM treatment eliminated residual lead iodide but failed to induce 001-plane oriented growth. These findings not only rule out chloride ion influence but also indicate that the controlled growth of perovskite originates from dual mechanisms: in-situ reactions between ClFACl and FAI, which facilitate phase transformation, and the preferential adsorption of active guanidine salt FA-Gua, which induces 001-plane oriented growth.

Theoretical calculation was carried out to estimate the binding energy (E_b) of FA-Gua on different facets of perovskite to investigate how FA-Gua interact with the lattice of $FAPbI_3$ perovskite along different facets and influence the subsequent crystalline orientation. To simplify the calculation, pure $FAPbI_3$ was employed as the calculation model. Configurations of FA-Gua combined on the (001), (011) and (111) facets were optimized to the lowest energy state, with the corresponding configuration and adsorption energies summarized in figure 2(e)-(h). The

results revealed a lower binding energy of −4.80 eV for FA-Gua on the (001) facet compared to −4.28 eV on the (011) facet and −3.73 eV on the (111) facet, suggesting a preferential interaction of FA-Gua on the (001) facet. Such preferential interaction could effectively reduce the surface energy of the (001) facet, promoting its stabilization and facilitating crystal growth in that direction [58,59]. Therefore, the mechanism of FA-Gua-induced crystal plane orientation growth is demonstrated in figure 2(i). The FA-Gua formed by the in-situ reaction of ClFACl and FAI effectively binds to the (001) facet through coordination and hydrogen bonding, thereby reducing the surface energy of the (001) crystal plane. During the annealing process, the adsorption of FA-Gua induces the preferential growth of the (001) crystal plane, while the growth of other crystal planes is relatively lagging [60].

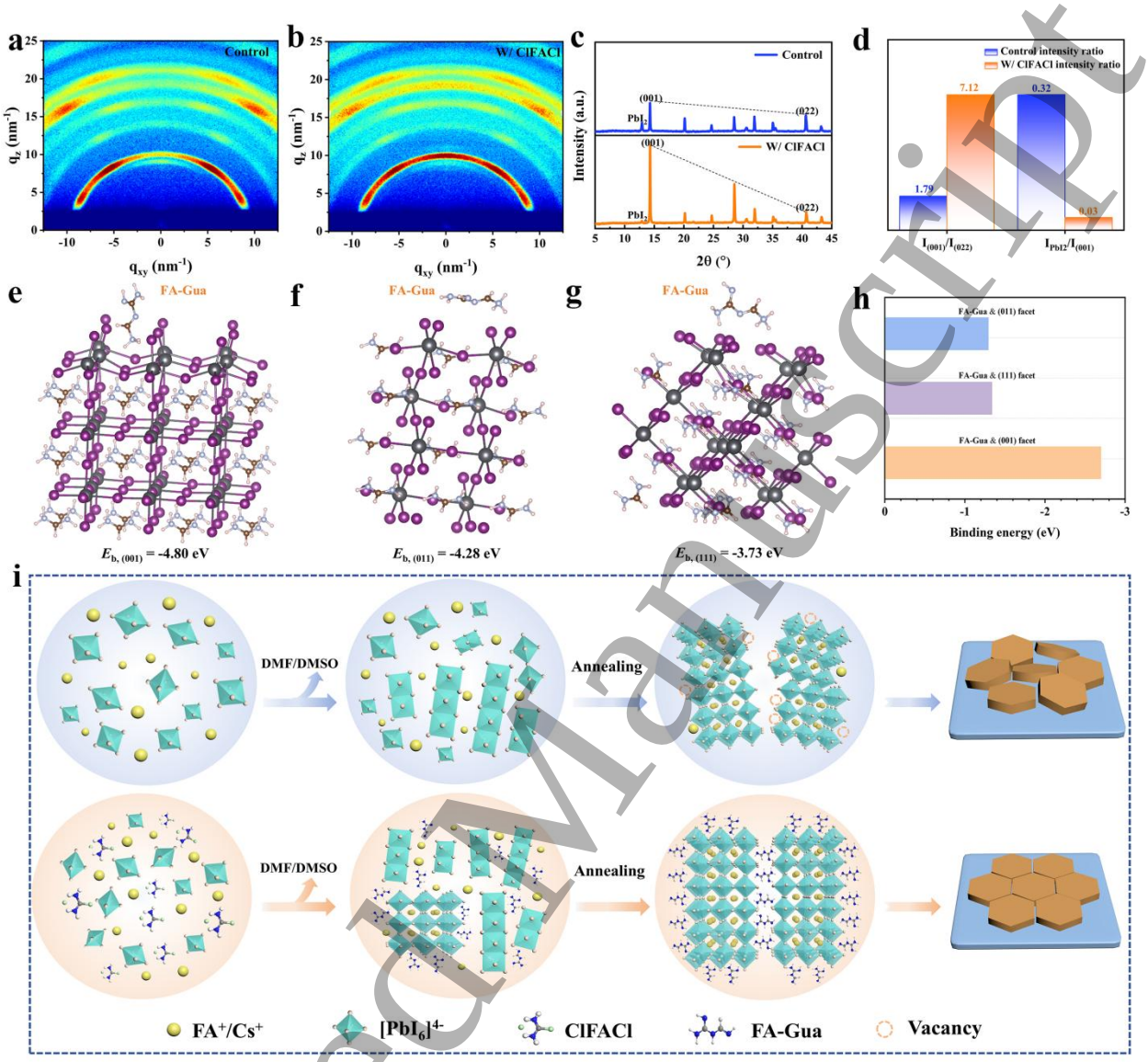

Figure 2. Observations on the in situ synthesis of FA-Gua to induce the oriented growth of films. (a) The XRD patterns of the perovskite films without and with ClFACl treatment. (b) Corresponding ratios of the intensity of (001)/(022) and (PbI_2)/(001) for the XRD patterns. (c, d) 2D GIWAXS patterns of perovskite films without and with ClFACl treatment. (e-g) Calculated binding energy (E_b) of FA-Gua binding on the e) (001) facet (E_b, (001)), (f) (011) facet (E_b, (011)) and g) (111) facet (E_b, (111)) of $FAPbI_3$. (h) Binding energy of FA-Gua in (100), (110) and (111)

of $FAPbI_3$ facets. (i) Schematic diagram of the nucleation and crystallization for the control and ClFACl-treated perovskite films.

Scanning electron microscopy (SEM) was applied to explore the effect of ClFACl additive on the morphology of perovskite films. As shown in figure 3(a) and 3(b), the ClFACl-treated film exhibited larger crystal size (figure S16) and flatter surface. For the cross-sectional SEM images (figure 3(c) and 3(d)), the ClFACl-treated perovskite film showed improved crystallization orientation and fewer grain boundaries. The in-situ formed FA-Gua interacted with (001) facet through coordination bonds, inducing the directional growth of the crystal. Subsequently, it diffuses to the grain boundaries and passivates the uncoordinated Pb^{2+} and halide vacancies at the grain boundaries through hydrogen bonds and coordination interactions.

Steady-state and time-resolved photoluminescence (PL and TRPL) measurements were used to reveal the carrier transfer and recombination mechanism. The PL spectra of the as-prepared perovskite films are displayed in figure 3(e), in which the PL intensity of ClFACl-treated perovskite film is remarkably enhanced compared with that of the control film, indicating the reduced traps in perovskite films with the introduction of ClFACl. The TRPL spectra of the perovskite films prepared on different substrates and fitted using a double exponential decay function are displayed in figure 3(f) and S17. As shown in figure 3(f), the ClFACl-treated film prepared on glass shows a prolonged average carrier lifetime compared with the control film, and the corresponding detailed parameters are summarized in Table S1. In addition, on $PC_{61}BM$/ITO and 2PACz/ITO, the ClFACl-treated perovskite film shows improved transporting ability of electrons (figure S17a and Table S2) and holes (figure S17b and Table S3), respectively. These results suggest that the as-formed active guanidine effectively passivates defects and improves

crystallinity of the perovskite film, which contribute to the suppression of nonradiative recombination and facilitate charge carrier transport.

Furthermore, selected area PL mapping measurement on both control and ClFACl-treated perovskite films was conducted to further verify the improvement of perovskite film crystallinity and the suppression of nonradiative recombination, as shown in figure 3(g) and 3(h). It can be observed that the perovskite film containing ClFACl shows higher PL intensity, indicating that the defects are passivated effectively. Meanwhile, as displayed in figure 3(i) and S18, the Kelvin probe force microscopy (KPFM) results demonstrate the ClFACl-treated perovskite film exhibits a more uniform and narrower distribution of surface contact potential difference (CPD) than that of the pristine one, indicating a reduced degree of energy disorder of the perovskite film surface [61-64]. Moreover, the ClFACl-treated perovskite film shows a lower average CPD (-183.4 mV) compared with that of pristine film (-145.4 mV), which is beneficial to reducing the hole-transport barrier of perovskite/HTL interface layer and facilitating efficient charge transfer.

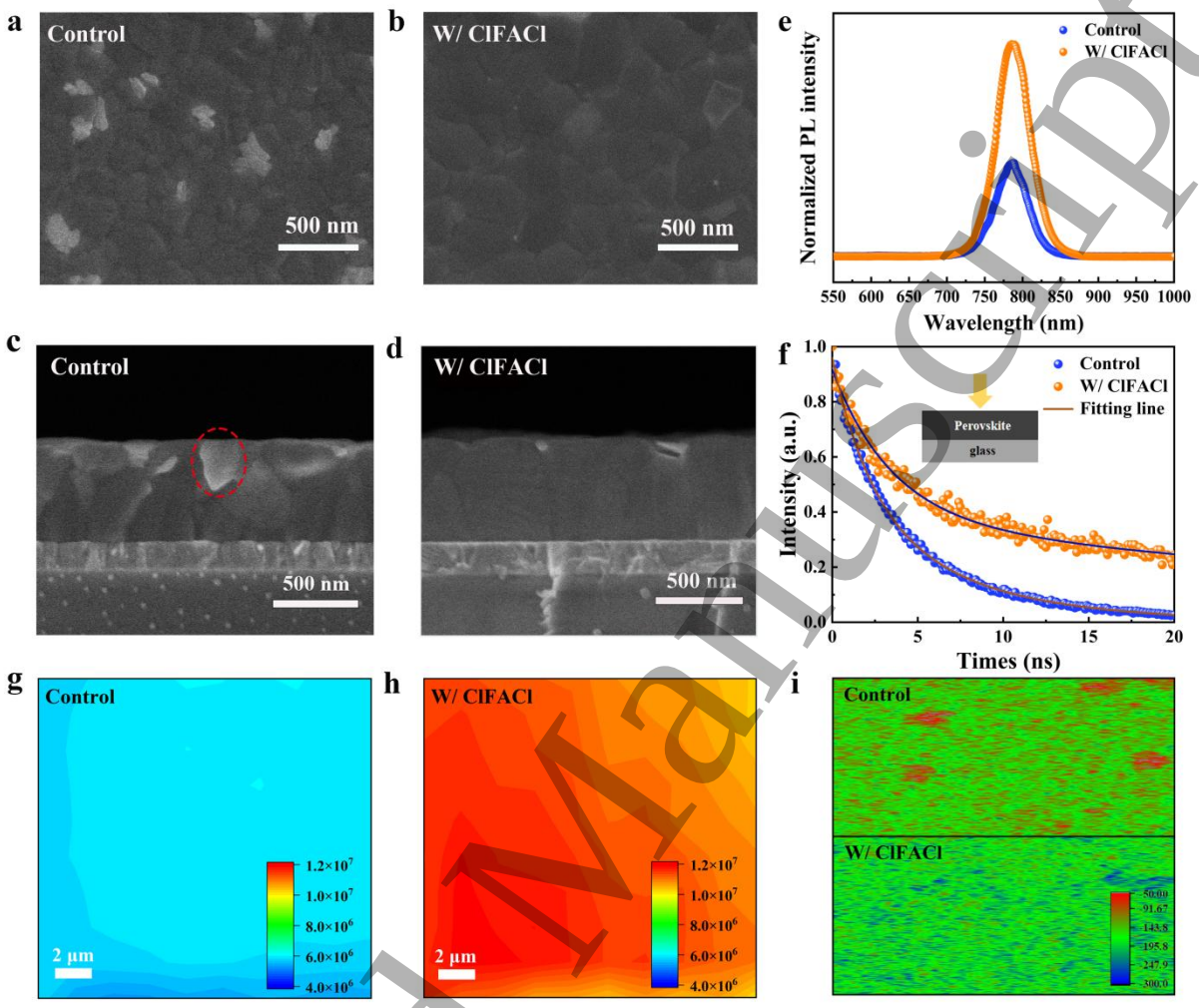

Figure 3. Comparison of the crystallinity and optical properties of thin films. (a-d) Top-view and cross-sectional SEM images of control and ClFACl-treated perovskite films. (e) Steady-state PL spectra of perovskite films without and with ClFACl treatment. (f) TRPL spectra of control and ClFACl-treated perovskite films based on glass. (g-h) PL mapping of control and ClFACl-treated perovskite films. (i) KPFM patterns of control and ClFACl-treated perovskite films.

Then we studied the effect of the strengthened intermolecular interactions in the interior of crystals and the suppression of defects with the in situ formation of FA-Gua on the stability enhancement of facet-oriented perovskite films. As displayed in figure S19, the ClFACl-treated

perovskite film shows a larger water contact angle (73°) compared to the control film (59°), indicating the released surface tension as well as the improvement of stability toward humidity of the perovskite film processed with ClFACl. In addition, the photographs of control and ClFACl-treated perovskite films heated at 80 °C in ambient air (40-60% RH) for 10 days are shown in figure 4(a). For the control film, a yellow phase appeared at the edge after heating for 9 days, and the film degraded severely after 15 days. However, the ClFACl-treated perovskite film remained in the black phase and slightly degraded around the edges after 15 days, showing excellent thermal and humid stability. Moreover, to systematically evaluate the influence of in situ formed FA-Gua on the stability of perovskite film, we recorded the decomposition process via SEM measurements. As exhibited in figure 4(b) and 4(c), after being heated under 80 °C in ambient air with 40-60% relatively humidity (RH) for 96 h, the control perovskite film degrades severely with PbI_2 flakes appeared on the surface, while he ClFACl-treated perovskite film shows little change (figure 4(c)).

Meanwhile, as shown by the XRD results (figure 4(d)), after 12 days of storage in the ambient air (25 °C, 60% RH), the control film exhibited enhanced peak intensity of PbI_2 (12.7°) and the δ-$FAPbI_3$ phase (11.8°), while the ClFACl-processed perovskite film maintained its black α-phase. We further probed the effect of ClFACl treatment on the enhancement of thermal stability of perovskite film under the condition of 60 °C in N_2 atmosphere for 18 days. As displayed in figure 4(e) and 4(f), the peak intensity of (001) and (022) crystal facets of the control perovskite film decreased along with an increase of PbI_2 peak intensity. For the ClFACl-treated perovskite film, there was negligible degradation of the (001) and (022) crystal facets, with a slight increase for the peak intensity of PbI_2. To evaluate the effectiveness of FA-Gua in preventing lead ion leakage from the perovskite film under extreme conditions, an acidic solution immersion test was

performed on unencapsulated perovskite films [65]. As shown in figure S20a, after being immersed in an acidic solution for 60 min, the control film completely degraded, while the ClFACl treated film remained in a stable black phase, indicating the FA-Gua can effectively prevent lead leakage. Meanwhile, we conducted an inductively coupled plasma mass spectrometry (ICP-MS) measurements on the leaching solution (figure S20b). The control film exhibited a high lead ion concentration of 0.015 μg/L, while the ClFACl-treated film showed minimal lead leakage of 0.0025 μg/L, indicating that the strong interaction of the active FA-Gua enhanced the hydrophobicity of the film and effectively inhibited its degradation.

The above results demonstrate that the ClFACl-treated films possessed excellent thermal and humid stability attributable to the strong hydrogen bonding and coordination interaction between the amino-groups-rich FA-Gua molecules and perovskite surface (figure 4(g)).

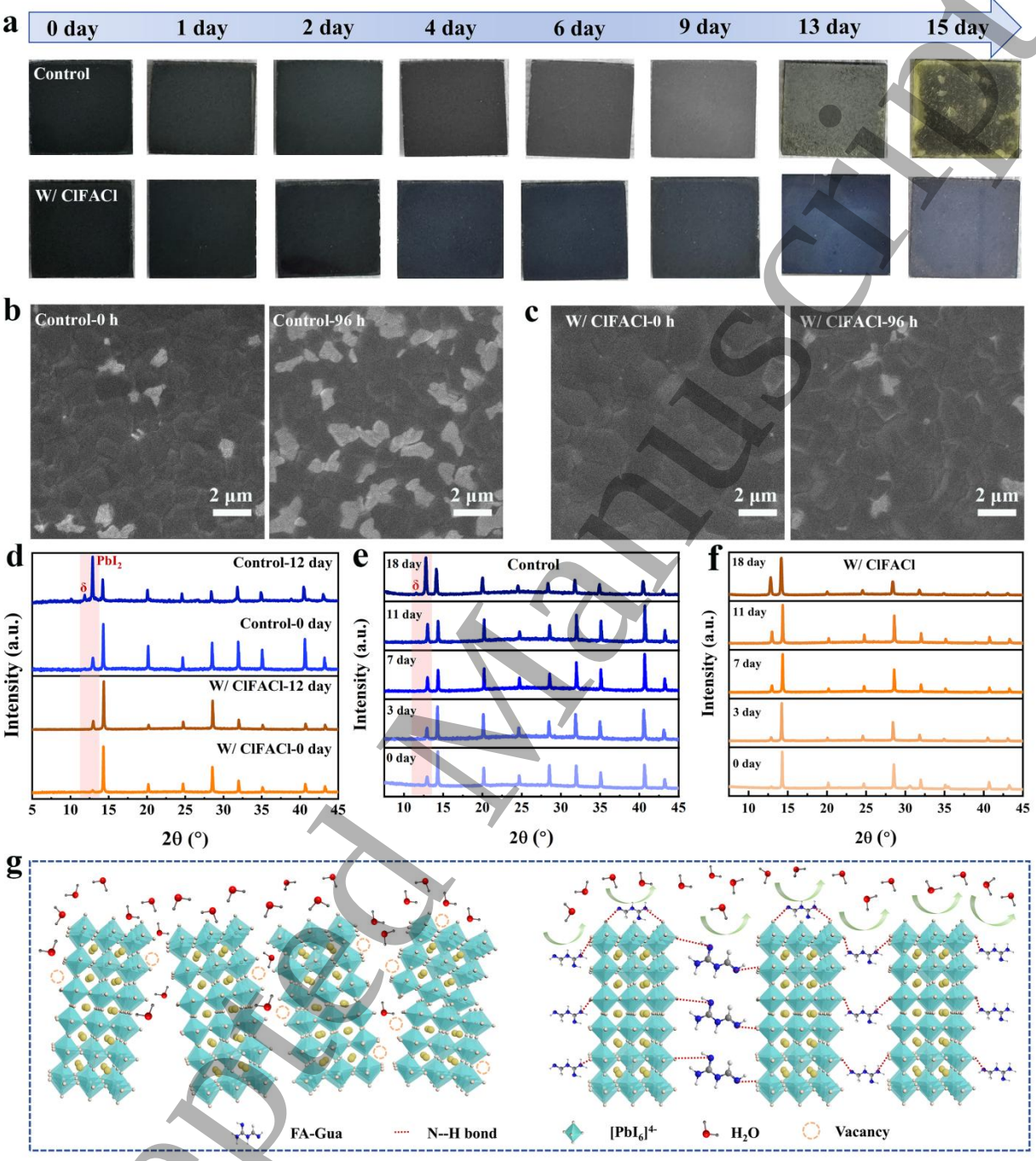

Figure 4. Enhanced intermolecular interactions improve the stability of perovskite films. (a) Photographs of control and ClFACl-treated perovskite films under 80 °C heating aging in ambient air (40-60% RH). (b-c) Surface SEM images of control and ClFACl-treated perovskite films before and after being heated at 80 °C in ambient air (40-60% RH). (d) XRD patterns of

control and ClFACl-treated perovskite films stored in ambient air (60% RH). (e-f) XRD patterns of control and ClFACl-treated perovskite films stored under 60 °C heating in N_2 glovebox for 18 days. (g) Schematic illustration of the decreased moisture sensitivity of perovskite crystals with the introduction of ClFACl and in situ synthesis of FA-Gua.

Inspired by the optimized crystallization orientation, reduced defects and enhanced stability of the perovskite film, we fabricated inverted p-i-n devices with the structure of ITO/2PACz/perovskite/$PC_{61}BM$/BCP/Ag to study the effect of in situ formed FA-Gua on photovoltaic performance, as illustrated in figure 5(a). As displayed in figure 5(b), the control device exhibits a highest PCE of 23.85%, with a V_{OC} of 1.16 V, a short circuit current density (J_{SC}) of 25.06 mA cm^{-2}, and a fill factor (FF) of 81.86%. In comparison, the ClFACl-treated devices show a champion PCE of 25.85%, along with an increased V_{OC} of 1.21 V, a J_{SC} of 25.76 mA cm^{-2} and an FF of 82.93%. In addition, compared with the pristine device, the hysteresis index of ClFACl-treated device decreased from 6.4% to 2.6% owing to the reduced defect state density (figure S21). The statistical box charts of PCE, V_{OC} and FF are shown in figure 5(c) and S22, in which the ClFACl-treated devices showed improved parameters.

Meanwhile, by comparing non-in situ and in situ reaction in perovskite precursor, we find that the in situ reaction can achieve low voltage loss and long-term working stability. Compared with the reported works, we used chloroformamidine hydrochloride (ClFACl) to in-situ react with FA cation to inhibit impurity intermediate phase in the perovskite film, and prepared high-quality and stable perovskite films by adjusting the phase transformation kinetics, resulting in PSCs with the lowest V_{OC} loss and the highest PCE (figure S23). Then, the corresponding external quantum efficiency (EQE) spectra of control and ClFACl-treated devices are shown in figure 5(d). The integrated J_{SC} of 23.52 and 24.50 mA cm^{-2} are consistent with the corresponding current density

versus voltage (*J-V*) results. Meanwhile, the ClFACl-treated device shows an excellent stable output efficiency under the maximum power point. As shown in figure 5(e), the PCE maintained at 25.48% with a stable output current density of 24.03 mA cm^{-2}.

The space-charge-limited current (SCLC) method was applied to quantify the effect of ClFACl treatment on the defect state density of perovskite films. As demonstrated in figure 5(f), for the hole-only devices, the ClFACl-treated perovskite film exhibited a lower trap density (2.49×1015 cm^{-3}) than the control device (3.86×1015 cm^{-3}). Meanwhile, for the electron-only device, the trap densities of perovskite films without and with ClFACl treatment were 3.86×1015 and 2.71×1015 cm^{-3}, respectively (figure S24). These results suggest that the in situ formed FA-Gua passivated defects in perovskite films effectively, which is beneficial to reducing charge-carrier recombination and improving the photoelectric performance of the devices. Electrochemical impedance spectroscopy (EIS) measurement was conducted to study the carrier transport and recombination behavior of the as-prepared devices. The corresponding nyquist plots and bode plots are displayed in figure S25. Upon the incorporation of ClFACl, the recombination resistance (R_{rec}) in the low-frequency region increased and the lifetime was prolonged, suggesting the suppressed defect-assisted charge recombination and improved charge transport in ClFACl-treated devices thanks to the reduction of defects.

To further reveal the carrier recombination mechanism in the control and ClFACl-treated devices, light intensity dependence of V_{OC} was measured. As shown in figure 5(g), the slop of ClFACl-treated device decreased to 1.32k_BT/q compared with that of the control one (1.56k_BT/q), indicating the effective suppression of non-radiative carrier recombination by the introduction of ClFACl. Furthermore, the effect of ClFACl treatment on internal carrier dynamics of devices were investigated by transient photovoltage (TPV) and transient photocurrent (TPC)

measurements. As shown in figure 5(h), the device treated by ClFACl exhibited a much longer photovoltage decay lifetime (227.87 μs) than the control device (80.53 μs). Meanwhile, the TPC decay curve of the ClFACl-treated device gives a carrier transfer time of 49.76 μs, which is shorter than that of the pristine one (88.61 μs, figure S26). The detailed parameters are summarized in Table S4 and Table S5. The in situ synthesis of active guanidine effectively suppressed carrier recombination and enhanced charge extraction, resulting in prolonged photovoltage decay lifetime and decreased carrier transfer time [66].

We conducted continuous maximum power point tracking (MPPT) tests on the control and the ClFACl-treated devices to examine the operational stability of the devices. As shown in figure S27, the results indicated that ClFACl-treated device maintained 90.14% of initial power conversion efficiency after 400 hours (~40% RH at room temperature, ISOS-L-1), while the control perovskite solar cell dropped to approximately 78.71%. In addition, we also conducted wet heat stability test on unencapsulated devices in the air environment. As shown in figure S28, under the conditions of temperature of 80 °C and 60% relative humidity, ClFACl-treated devices maintained 90% of the initial efficiency after 200 hours, while the lifespan of the control devices was significantly shortened. This indicates that the generation of active guanidine salts enhances the intermolecular interactions within the perovskite film, thereby significantly improving the wet heat stability of the devices. Furthermore, the long-term storage stability of unencapsulated devices with and without ClFACl treatment was measured under N_2 atmosphere. As displayed in figure 5(i), after 2000 h, the ClFACl-treated device maintained 95% of its initial PCE, while PCE of the control device decayed to 78% of the initial value. This result confirms the effectiveness of the in situ synthesized FA-Gua on the stability enhancement of PSCs.

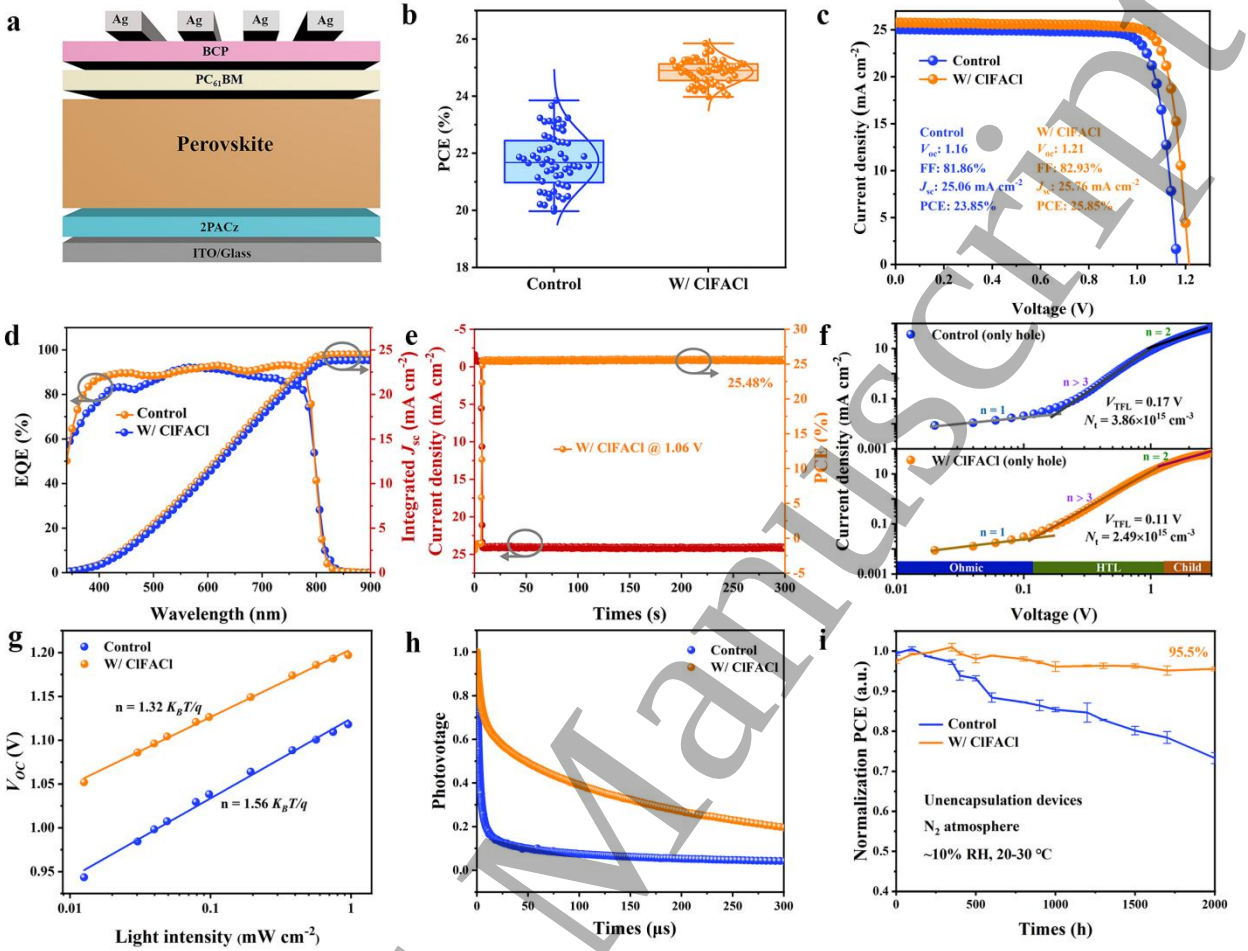

Figure 5. Device performances and carrier recombination statistics. (a) Schematic illustration of device structure of p-i-n single-junction solar cell. (b) PCE distribution of pristine and ClFACl treated devices. (c) *J-V* curves of champion PSCs with and without ClFACl treatment. (d) EQE spectra and the corresponding integrated J_{SC} curve of the ClFACl-treated device. (e) Stabilized power output of the ClFACl-treated device tracked at the maximum power point. (f) Dark *J-V* characteristics of hole-only devices with and without ClFACl treatment. (g) Light dependence of V_{OC} of the devices with and without ClFACl treatment. (h) TPV curves of the devices with and without ClFACl treatment. (i) Long-term stability tests of unencapsulated control and ClFACl-treated devices under N_2 atmosphere.

4. Conclusions

In summary, ClFACl is introduced to the perovskite precursor solution to induce the formation of active guanidine through in situ reaction between ClFACl and FAI. Detailed characterizations demonstrated that the as-synthesized FA-Gua not only optimized the crystallization kinetics of perovskite and promoted the generation of α-$FAPbI_3$, but also induced the formation of (001) facet dominant perovskite film with higher crystallinity. Benefiting from the strong interaction between nitrogenous groups and perovskite, the generated active guanidine strongly passivated the defects of perovskite film and suppressed carrier recombination, thus improved the humidity and thermal stability of ClFACl-treated perovskite film and photovoltaic performance of devices. The ClFACl-treated devices gave an optimized PCE of 25.85%, along with an excellent V_{OC} of 1.21 V and an improved FF of 82.93%. In addition, the unencapsulated ClFACl-treated devices retained 95% of the initial PCE after 2000 h storage. Our work provides a reliable way for further understanding the interaction between additives and perovskite precursors, promoting the construction of high-efficiency and stable PSCs.

5. Future perspectives

Looking ahead, this additive-engineering platform-where chloroformamidinium hydrochloride (ClFACl) is judiciously deployed to orchestrate an in-situ, crystal-face-selective reaction-sets a new benchmark for defect-scarce, orientation-ordered perovskite films. By precisely steering the phase-transformation kinetics, the approach not only suppresses parasitic intermediates but also accelerates the formation of thermodynamically and kinetically favored crystal facets. Consequently, perovskite solar cells exhibit high power-conversion efficiencies alongside enhanced ambient and thermal stability. Beyond laboratory-scale devices, the methodology is

intrinsically scalable and compatible with roll-to-roll processing, positioning it as a robust pathway toward industrial-scale manufacturing of next-generation, high-performance photovoltaics.

Acknowledgments

We thank Dongyue Hu of the Core Facilities for Life and Environmental Sciences, State Key laboratory of Microbial Technology of Shandong University for ^{1}H NMR and XRD analysis. The work was supported by National Natural Science Foundation of China (No. 52202042, No. 21975273, No. 52472048, No. 22405162), Natural Science Foundation of Shandong Province (No. ZR2021QE191), the Major Basic Research Project of Natural Science Foundation of Shandong Province (No. ZR2022ZD36), Guangdong Basic and Applied Basic Research Foundation (No. 2024A1515012432, No. 2022A1515240007), Special Fund for the Sci-tech Innovation Strategy of Guangdong Province (STKJ202209083), the China Postdoctoral Science Foundation (No. 2023M732036, 2023M732057), China National Postdoctoral Program for Innovative Talents (Certificate Number: BX20230202), Young Elite Scientists Sponsorship Program by CAST (2022QNRC001), Scientific Research Starting Foundation of Outstanding Young Scholar of Shandong University, and the Future Young Scholars Program of Shandong University.

Conflict of interest

The authors declare no conflict of interest

Authors contribution

Jiajia Du: Writing – original draft, Formal analysis, Data curation. **Yilin Chang:** Methodology, Formal analysis. **Le Liu:** Conceptualization, Methodology, Formal analysis. **Zhibin Yu:**

Supervision, Software. **Qinglin Du:** Investigation. **Wenfeng Yang:** Data curation. **Yuan Qiu:** Software, Data curation. **Fushen Lu:** Writing – review & editing. **Tonggang Jiu:** Writing – review & editing, Validation, Funding acquisition. **Huanqi Cao:** Writing – review & editing, Validation, Funding acquisition.

ORCID iD

Huanqi Cao https://orcid.org/0000-0002-3092-1578.

References

[1] Dong H, Ran C, Gao W, Li M, Xia Y, and Huang W 2023 Metal Halide Perovskite for next-generation optoelectronics: progresses and prospects *eLight.* 3 3.

[2] Liu A, Xi J, Cen H, Dai J, Yang Y, Liu C, Guo S, Li X, Guo X, Yang F et al 2025 Roadmap on metal-halide perovskite semiconductors and devices *Mater. Today Electronics* 11 100138.

[3] Zhang S, Ye F, Wang X, Chen R, Zhang H, Zhan L, Jiang X, Li Y, Ji X, Liu S, Yu M et al 2023 Minimizing buried interfacial defects for efficient inverted perovskite solar cells *Science.* 380 404-409.

[4] Liang Z, Zhang Y, Xu H, Chen W, Liu B, Zhang J, Zhang H, Wang Z, Kang D H and Zeng J 2023 Homogenizing out-of-plane cation composition in perovskite solar cells *Nature.* 624 557-563.

[5] Zhang Z, Qiao L, Meng K, Long R, Chen G, and Gao P 2023 Rationalization of passivation strategies toward high-performance perovskite solar cells *Chem. Soc. Rev*. 52 163-195.

[6] Li B, Gao D, Sheppard S.A., Tremlett W.D.J., Liu Q, Li Z, White A J P, Brown R K, Sun X, Gong J, et al 2024 Highly Efficient and Scalable p-i-n Perovskite Solar Cells Enabled by Poly-metallocene Interfaces *J. Am. Chem. Soc*. 146 13391-13398.

[7] Liu S, Li J, Xiao W, Chen R, Sun Z, Zhang Y, Lei X, Hu S, Kober-Czerny M, Wang J, et al 2024 Buried interface molecular hybrid for inverted perovskite solar cells *Nature*. 632 536-542.

[8] Duan T, You S, Chen M, Yu W, Li Y, Guo P, Berry J J, Luther J M, Zhu K, and Zhou Y 2024 Chiral-structured heterointerfaces enable durable perovskite solar cells *Science*. 384 878-884.

[9] NREL, Best Research-Cell Efficiencies Chart, http://www.nrel.gov/pv/cell/efficiency.html..

[10] Chen H, Liu C, Xu J, Maxwell A, Zhou W, Yang Y, Zhou Q, Bati A S R, Wan H,Wang Z et al 2024 Improved charge extraction in inverted perovskite solar cells with dual-site-binding ligands *Science*. 384 189-193.

[11] Zuo W, Fu W, Wang K, Das C, Byranvand M M, Wang K, Chaudhary A, Lim J, Li M, and Saliba M 2024 Crystallization dynamics and stabilization of $FAPbI_3$ single-phase perovskite *Energy Environ. Sci.* 17 1407-1415.

[12] Li B, Li S, Gong J, Wu X, Li Z, Gao D, Zhao D, Zhang C, Wang Y, and Zhu Z 2024 Fundamental understanding of stability for halide perovskite photovoltaics: The importance of interfaces *Chem*. 10 35-47.

[13] Li N, Zhu Z, Chueh C C, Liu H, Peng B, Petrone A, Li X, Wang L and Jen A K Y 2016 Mixed Cation $FA_xPEA_{1-x}PbI_3$ with Enhanced Phase and Ambient Stability toward High-Performance Perovskite Solar Cells *Adv. Energy Mater*. 7 1601307.

[14] Huang Y, Lei X, He T, Jiang Y and Yuan M 2021 Recent Progress on Formamidinium-Dominated Perovskite Photovoltaics *Adv. Energy Mater*. 12 2100690.

[15] Yang F, Dong L, Jang D, Tam K, Zhang K, Li N, Guo F, Li C, Arrive C, Bertrand M et al 2020 Fully Solution Processed Pure α-Phase Formamidinium Lead Iodide Perovskite Solar Cells for Scalable Production in Ambient Condition *Adv. Energy Mater*. 10 2001869.

[16] Zuo W, Fu W, Wang K, Das C, Byranvand M, Wang K, Chaudhary A, Lim J, Li M and Saliba M 2024 Crystallization dynamics and stabilization of $FAPbI_3$ single-phase perovskite *Energy Environ. Sci*. 17 1407-1415.

[17] Wu Z, Sang S, Zheng J, Gao Q, Huang B, Li F, Sun K, and Chen S 2024 Crystallization Kinetics of Hybrid Perovskite Solar Cells *Angew Chem. Int. Ed.* 63 e202319170.

[18] Yin Q, Chen T, Xie J, Lin R, Liang J, Wang H, Luo Y, Zhou S, Li H, Wang Z et al 2024 Unveiling the Effect of Cooling Rate on Grown-in Defects Concentration in Polycrystalline Perovskite Films for Solar Cells with Improved Stability *Adv. Mater*. 36 e2405840.

[19] Sanchez S, Pfeifer L, Vlachopoulos N, and Hagfeldt A 2021 Rapid hybrid perovskite film crystallization from solution *Chem. Soc. Rev*. 50 7108-7131.

[20] Zhang X, Shang C, Wang C, Zhao W, Tao C, Wang S, Zhang X, Han R, Zhou B, Qu D et al 2014 Preferred Crystallographic Orientation via Solution Bathing for High-Performance Inverted Perovskite Photovoltaics *Adv. Funct. Mater.* 34 2407732.

[21] Foley B J, Cuthriell S, Yazdi S, Chen A Z, Guthrie S M, Deng X, Giri G, Lee S H, Xiao K, Doughty B et al 2018 Impact of Crystallographic Orientation Disorders on Electronic Heterogeneities in Metal Halide Perovskite Thin Films *Nano Lett*. 18 6271-6278.

[22] Jariwala S, Sun H, Adhyaksa G W P, Lof A, Muscarella L A, Ehrler B, Garnett E C and Ginger D S 2019 Local Crystal Misorientation Influences Non-radiative Recombination in Halide Perovskites *Joule*. 3 3048-3060.

[23] Park J, Kim J, Yun H S, Paik M J, Noh E, Mun H J, Kim M G, Shin T J, and Seok S I 2023 Controlled growth of perovskite layers with volatile alkylammonium chlorides *Nature*. 616 724-730.

[24] Liu X, Jiang X, Yin Y, Zhang J, Tian H, Guo J, Guo X and Li C 2024 Dominating (111) facets with ordered stacking in perovskite films *Energy Environ. Sci*. 17 6058-6067.

[25] McKenna K P 2018 Electronic Properties of (111) Twin Boundaries in a Mixed-Ion Lead Halide Perovskite Solar Absorber *ACS Energy Lett*. 3 2663-2668.

[26] Tan C S, Hou Y, Saidaminov M I, Proppe A, Huang Y S, Zhao Y, Wei M, Walters G, Wang Z, Zhao Y et al 2020 Heterogeneous Supersaturation in Mixed Perovskites *Adv. Sci.* 7 1903166.

[27] Li W, Rothmann M U, Zhu Y, Chen W, Yang C, Yuan Y, Choo Y Y, Wen X, Cheng Y-B, Bach U et al 2012 The critical role of composition-dependent intragrain planar defects in the performance of $MA_{1-x}FA_xPbI_3$ perovskite solar cells. *Nat. Energy.* 6 624-632.

[28] Jiang X, Liu B, Wu X, Zhang S, Zhang D, Wang X, Gao S, Huang Z, Wang H, Li B et al 2014 Top-Down Induced Crystallization Orientation toward Highly Efficient p-i-n Perovskite Solar Cells. *Adv. Mater*. 36 e2313524.

[29] Meng K, Wang X, Xu Q, Li Z, Liu Z, Wu L, Hu Y, Liu N, and Chen G 2019 In Situ Observation of Crystallization Dynamics and Grain Orientation in Sequential Deposition of Metal Halide Perovskites. *Adv. Funct. Mater.* 29 1902319.

[30] Ma C, Kang M C, Lee S H, Zhang Y, Kang D H, Yang W, Zhao P, Kim S W, Kwon S J, Yang C W et al 2023 Facet-Dependent Passivation for Efficient Perovskite Solar Cells. *J. Am. Chem. Soc*. 145 24349-24357.

[31] Lee J, Shin Y S, Oleiki E, Seo J, Roe J, Lee D, Lee Y, Song T, Jang H, Song J W et al 2024 Constructing orderly crystal orientation with a bidirectional coordinator for high efficiency and stable perovskite solar cells *Energy Environ. Sci*. 17 6003-6012.

[32] Ma C, Grätzel M, and Park N-G 2022 Facet Engineering for Stable, Efficient Perovskite Solar Cells *ACS Energy Lett.* 7 3120-3128.

[33] Ma C, Kang M-C, Lee S-H, Kwon S J, Cha H-W, Yang C-W and Park N-G 2022 Photovoltaically top-performing perovskite crystal facets *Joule*. 6 2626-2643.

[34] Lin Q, Armin A, Nagiri R C R, Burn P L and Meredith P 2014 Electro-optics of perovskite solar cells *Nat. Photon*. 9 106-112.

[35] Zheng X, Hou Y, Bao C, Yin J, Yuan F, Huang Z, Song K, Liu J, Troughton J, Gasparini N et al 2020 Managing grains and interfaces via ligand anchoring enables 22.3%-efficiency inverted perovskite solar cells *Nat. Energy.* 5 131-140.

[36] Ma C, Eickemeyer F T, Lee S.H, Kang D.H., Kwon S J, Grätzel M and Park N-G 2023 Unveiling facet-dependent degradation and facet engineering for stable perovskite solar cells *Science*. 379 173-178.

[37] Luo C, Zheng G, Gao F, Wang X, Zhao Y, Gao X and Zhao Q 2022 Facet orientation tailoring via 2D-seed- induced growth enables highly efficient and stable perovskite solar cells *Joule*. 6 240-257.

[38] Kim D, Yun J-H, Lyu M, Kim J, Lim S, Yun J S, Wang L and Seidel J 2019 Probing Facet-Dependent Surface Defects in $MAPbI_3$ Perovskite Single Crystals *J. of Phys. Chem. C*. 123 14144-14151.

[39] Wang Y, Shi Z, Wang Y, Zhang J, Zhang X, Li X, Wang H, Li C, Wang J, Zhang H et al 2024 Highly Oriented $FAPbI_3$ via 2D Ruddlesden Popper Perovskite Template Growth *Adv. Energy Mater.* 14 2401721.

[40] Xu Z, Liu Z, Li N, Tang G, Zheng G, Zhu C, Chen Y, Wang L, Huang Y, Li L et al 2019 A Thermodynamically Favored Crystal Orientation in Mixed Formamidinium/Methylammonium Perovskite for Efficient Solar Cells *Adv. Mater*. 31 e1900390.

[41] Kim W, Jung M S, Lee S, Choi Y J, Kim J K, Chai S U, Kim W, Choi D G, Ahn H, Cho J H et al 2017 Oriented Grains with Preferred Low-Angle Grain Boundaries in Halide Perovskite Films by Pressure-Induced Crystallization *Adv. Energy Mater*. 8 1702369.

[42] Wang K, Wu C, Hou Y, Yang D, Ye T, Yoon J, Sanghadasa M and Priya S 2022 Isothermally crystallized perovskites at room-temperature *Energy Environ. Sci*. 13 3412-3422.

[43] Wang J, Yuan L, Luo H, Duan C, Zhou B, Wen Q and Yan K 2022 Ambient air processed highly oriented perovskite solar cells with efficiency exceeding 23% via amorphous intermediate *Chem. Eng. J*. 446 136968.

[44] Qu S, Huang H, Wang J, Cui P, Li Y, Wang M, Li L, Yang F, Sun C, Zhang Q et al 2024 Revealing and Inhibiting the Facet-related Ion Migration for Efficient and Stable Perovskite Solar Cells *Angew. Chem. Int. Ed*. 64 e202415949.

[45] Zhou W, Tai S, Li Y, Fu H and Zheng Q 2024 Achieving High-Quality Perovskite Films with Guanidine-Based Additives for Efficient and Stable Methylammonium-Free Perovskite Solar Cells *Adv. Funct. Mater.* 34 2407897.

[46] Baeten M and Maes B U W 2016 Guanidine Synthesis: Use of Amidines as Guanylating Agents *Adv. Synth. Catal*. 358 826-833.

[47] Liu Z, Liu T, Li M, He T, Guo G, Liu P, Chen T, Yang J, Qin C, Dai X et al 2024 Eliminating Halogen Vacancies Enables Efficient MACL-Assisted Formamidine Perovskite Solar Cells *Adv. Sci.* 11 e2306280.

[48] Wang S, Li M, Jiang Y, and Hu J 2023 Instability of solution-processed perovskite films: origin and mitigation strategies *Mater. Futures* 2 012102.

[49] Li M, Ma X, Fu J, Wang S, Wu J, Long R, and Hu J 2024 Molecularly tailored perovskite/poly(3- hexylthiophene) interfaces for high-performance solar cells *Energy Environ. Sci.*, 17, 5513-5520.

[50] Li M, Gong X, Wang S, Li L, Fu J, Wu J, Tan Z, and Hu J 2024 Facile Hydrogen-Bonding Assisted Crystallization Modulation for Large-area High-quality $CsPbI_2Br$ Films and Efficient Solar Cells *Angew. Chem. Int. Ed.* 63, e202318591.

[51] Xu Z, Lu D, Dong X, Chen M, Fu Q and Liu Y 2021 Highly Efficient and Stable Dion-Jacobson Perovskite Solar Cells Enabled by Extended pi-Conjugation of Organic Spacer *Adv. Mater*. 33 e2105083.

[52] Dong H, Huang R, Gao W, Li W, Ran X, Chao L, Wang X, Zhou Y, Wu Z, Chen Y et al 2025 Decoupling Nucleation and Growth of Crystal for DMSO-Free Self-Assembly Tin Perovskite Films and Their Optoelectronic Application *Adv. Funct. Mater*. 35 2420593.

[53] Cao L, Tong Y, Ke Y, Chen Y, Li Y, Wang H and Wang K 2024 Dual Buried Interface Engineering for Improving Air-Processed Inverted $FAPbI_3$ Perovskite Solar Cells *ACS Appl. Mater. Interfaces.* 16 66865–66873.

[54] Bi C, Wang Q, Shao Y, Yuan Y, Xiao Z and Huang J 2015 Non-wetting surface-driven high-aspect-ratio crystalline grain growth for efficient hybrid perovskite solar cells *Nat. Commun*. 6 7747.

[55] Sun X, Li D, Zhao L, Zhang Y, Hu Q, Russell T P, Liu F, Wei J and Li H 2023 (111)-Dominated Perovskite Films by Antisolvent Engineering *Adv. Mater.* 35 e2301115.

[56] Toby B 2006 R factors in Rietveld analysis: How good is good enough? *Powder Diffr*. 21 67-70.

[57] Yang J, Wang Z, Zhao X, Gao W, Xing G, Wang X, Wang L, Li C, Wang Y, Ren Y et al 2025 Guiding vertical growth and improving the buried interface of Pb-Sn perovskite films with 2D perovskite seeds for efficient narrow-bandgap perovskite solar cells and tandems *Energy Environ. Sci.,* 18 2883-2894.

[58] Li S, Xia J, Wen Z, Gu H, Guo J, Liang C, Pan H, Wang X and Chen S 2023 The Formation Mechanism of (001) Facet Dominated α -$FAPbI_3$ Film by Pseudohalide Ions for High-Performance Perovskite Solar Cells *Adv. Sci.* 10 2300056.

[59] Li X, Gao S, Wu X, Liu Q, Zhu L, Wang C, Wang Y, Liu Z, Chen W, Li X et al 2024 Bifunctional ligand-induced preferred crystal orientation enables highly efficient perovskite solar cells *Joule*. 8 3169-3185.

[60] Wu J, Zhang W, Wang Q, Liu S, Du J, Mei A, Rong Y and Hu Y 2020 A favored crystal orientation for efficient printable mesoscopic perovskite solar cells *J. Mater. Chem. A.* 8 11148-11154.

[61] Wang J, Pan Y, Zhou Z, Zhou Q, Liu S, Zhang J, Shi C, Chen R, Zhao Z, Cai Z et al 2024 Bimolecular Crystallization Modulation Boosts the Efficiency and Stability of Methylammonium - Free Tin-Lead Perovskite and All - Perovskite Tandem Solar Cells *Adv. Energy Mater.* 36 2402171.

[62] Ray Chowdhuri A, Bhattacharya D and Sahu S K 2016 Magnetic nanoscale metal organic frameworks for potential targeted anticancer drug delivery, imaging and as an MRI contrast agent *Dalton transa*. 45 2963-2973.

[63] Lee S J, Heo J H and Im S H 2020 Large-Scale Synthesis of Uniform PbI_2(DMSO) Complex Powder by Solvent Extraction Method for Efficient Metal Halide Perovskite Solar Cells *ACS Appl. Mater. Interfaces*. 12 8233-8239.

[64] Bu T, Li J, Li H, Tian C, Su J, Tong G, Ono L K, Wang C, Lin Z, Chai N et al 2021 Lead halide – templated crystallization of methylamine-free perovskite for efficient photovoltaic modules *Science*. 372 1327-1332.

[65] Wu P, Heo J and Zhang F 2024 Lead chemisorption: Paving the last step for industrial perovskite solar cells. *Nano res. energy* 3 e9120093.

[66] Zhu X, Gu C, Cheng Y, Lu H, Wang X, Ran G, Zhang Z, Tang W, Liu Y and Bo Z 2025 3D-Architectured Acceptor with High Photoluminescence Quantum Yield and Moderate Crystallinity for High-efficiency Organic Solar Cells with Low Voltage Loss *Adv. Mater*. 37 2507529.